Pergamon

Int. J. Heat Mass Transfer. Vol. 41, No. 17, pp. 2601–2617, 1998

Printed in Great Britain
0017–9310/98 $19.00+0.00

PII: S0017–9310(97)00326–8

Direct numerical simulations of evaporating droplet dispersion in forced low Mach number turbulence

F. MASHAYEK†

Department of Mechanical Engineering, University of Hawaii at Manoa, 2540 Dole Street, Honolulu, HI 96822, U.S.A.

(*Received* 17 *June* 1997 *and in final form* 9 *October* 1997)

Abstract—Dispersion of evaporating droplets in forced low Mach number isotropic turbulence is studied using direct numerical simulation (DNS). The carrier phase is treated in the Eulerian frame, the droplets are tracked in the Lagrangian frame, and a (realistic) two-way coupling is considered. The results of the simulations are used to investigate the effects of the initial droplet time constant, the initial mass loading ratio, the initial droplet temperature, the latent heat of evaporation, the boiling temperature, and the initial vapor mass fraction on the droplet size, the temperature fields, and the vapor mass fraction. The DNS results indicate that the evaporation rate is nonlinear during the early times. The pdfs of the droplet diameter are skewed towards smaller droplets, however, they may be approximated as Gaussian for small mass loading ratios. An examination of the mean vapor mass fraction indicates that the mixture becomes nearly saturated at long times. The evolution of the fluctuating vapor mass fraction is investigated by considering the transport equation for the variance of this quantity. © 1998 Elsevier Science Ltd. All rights reserved.

1. INTRODUCTION

One of the most versatile and efficient means for combusting liquid fuels is via spray of the fuel into an oxidizer gas. Utilized in a variety of devices, spray combustion involves the atomization of the liquid fuel into droplets, the evaporation of these droplets, and finally the chemical reaction of the fuel vapor with the oxidizer. These stages have been subjects of numerous investigations within the past five decades. However, despite significant progress in predicting the overall performance of the spray, there are still many unresolved issues pertaining to each of the above-mentioned processes. Due to lack of sufficient information, most of the treatments of the spray, one way or the other, resort to *ad hoc* assumptions. For instance, while many of these treatments involve assumptions regarding droplet size distribution in various regions of the spray, accurate information on the 'form' of these distributions is very scarce. Motivated by these observations, in this paper we deal with one of the primary, and yet unresolved, issues in the spray combustion, namely the dispersion and polydispersity of evaporating droplets in turbulent flows. The specific objective is to use the result of the numerical simulations to gain further insight into the evolution of the two-phase flow. The turbulence is simulated by direct numerical simulation (DNS) which allows us to resolve all the scales of the flow without resorting to turbulence models. The effects of density and temperature variations are accounted for by considering compressible flows. The use of the droplet equations, which are primarily derived for steady incompressible flows, is justified by considering droplet sizes smaller than the Kolmogorov length scale and low Mach number flows.

The implementation of DNS in particle-laden flows is pioneered by Riley and Patterson [1] and since then it has been used by many others [2–5]; for recent reviews see McLaughlin [6] and Mashayek *et al.* [7]. However, most of the contributions have concentrated on solid particle dispersion; it has been only recently that we [8] conducted DNS of evaporating droplets in turbulent flows. This study has been very instructive in exhibiting many important features of polydispersity. However there are several restrictive simplifications invoked in this work which limits the generality and applicability of the DNS generated results. These are, specifically, the one-way coupling of the two phases and the assumption of incompressible flow. The chief objective of the present work is to expand upon the formulation of Mashayek *et al.* [8]; and relax both of the aforementioned assumptions. The resulting formulation provides a more realistic framework for turbulent spray analysis.

2. FORMULATION AND METHODOLOGY

Since this is the first attempt in DNS of the evaporating droplet dispersion in turbulent flows with two-

† Author to whom correspondence should be addressed. Tel.: 001 808 956 9693. Fax: 001 808 956 2373. E-mail: mashaye@wiliki.eng.hawaii.edu.

NOMENCLATURE

B	$(T^*-T_d)/\lambda$ transfer number
C_l	specific heat of the liquid
C_p	specific heat of the carrier phase
d_d	droplet diameter
E_I	internal energy of the carrier phase
E_K	$\frac{1}{2}\rho u_i u_i$ kinetic energy of the carrier phase
E_T	E_I+E_K total energy of the carrier phase
$E_Y(k)$	power spectrum of the vapor mass fraction
f_1	$(1+0.15Re_d^{0.687})/(1+B)$
f_2	$Nu/3\,Pr$
f_3	$\rho^* Sh\,\lambda/3\,Sc$
f_4	$\pi(18/\rho_d)^{0.5}(\rho^* Sh/Re_f^{1.5}\,Sc)$
$\mathscr{F}_i$	a zero-mean solenoidal random force
h	specific enthalpy
k	wavenumber
L_f	reference length
L_v	latent heat of vaporization of the liquid
m_d	mass of the droplet
M_f	$U_f/\sqrt{\gamma RT_f}$ reference Mach number
n_d	number of droplets within the cell volume
N	number of collocation points in each direction
N_d	total number of droplets
Nu	$(2+0.6Re_d^{0.5}\,Pr^{0.33})/(1+B)$ Nusselt number
p	pressure of the carrier phase
Pr	$C_p\mu/\kappa$ Prandtl number
R	gas constant
Re_d	$Re_f\rho^* d_d\lvert u_i^*-v_i\rvert$ droplet Reynolds number
Re_f	$\rho_f U_f L_f/\mu$ reference Reynolds number
S_d	droplet source term [equation (15)]
S_{ij}	$\frac{1}{2}(\partial u_i/\partial x_j+\partial u_j/\partial x_i)$ rate-of-strain tensor
$\mathscr{S}_m$, $\mathscr{S}_{ui}$, $\mathscr{S}_e$	coupling source/sink terms
Sc	$\mu/\rho\Gamma$ Schmidt number
Sh	$2+0.6Re_d^{0.5}\,Sc^{0.33}$ Sherwood number
t	time
T	temperature
T_B	boiling temperature of the liquid
u_i	velocity of the carrier phase in direction x_i $(i=1,2,3)$
U_f	reference velocity
v_i	velocity of the droplet in the direction x_i
x_i	spatial coordinates, $i=1,2,3$
X_i	position of the droplet, $i=1,2,3$
Y	vapor mass fraction.

Greek symbols

γ	ratio of the specific heats of the carrier gas
Γ	binary mass diffusivity coefficient
δ_{ij}	Kronecker delta function
δx	node spacing
$\delta\mathscr{V}$	cell volume
Δ	$\partial u_j/\partial x_j$ diltatation
ε	dissipation rate
κ	thermal conductivity of the carrier phase
λ	L_v/C_pT_f normalized latent heat of evaporation
λ_Y	Taylor microscale of the vapor mass fraction
μ	viscosity of the carrier phase
ρ	density
τ_d	$Re_f\rho_d d_d^2/18$ droplet time constant
τ_k	Kolmogorov timescale
ϕ_m	mass loading ratio.

Subscripts

0	initial value (at $t=0$)
d	droplet properties
f	reference properties for normalization
g	carrier gas
l	liquid phase
rms	root mean square
s	surface of the droplet
v	vapor
Y	vapor mass fraction.

Superscripts

$'$	Reynolds averaged fluctuating quantity
$''$	Favre averaged fluctuating quantity
*	Carrier phase properties at the droplet location.

Symbols

$\langle\,\rangle$	Eulerian ensemble average over the number of collocation points
$\langle\langle\,\rangle\rangle$	Lagrangian ensemble average over the number of droplets.

way coupling, the problem is formulated based on models and correlations which are relatively well-established. Also, due to the large number of parameters involved in the problem, and in order to simplify the analysis, the buoyancy effects are not included. We consider the motion of a large number of droplets (dispersed phase) in a turbulent flow (carrier phase). The transport of the carrier phase is con-

sidered in the Eulerian frame; whereas the dispersed phase is treated in the Lagrangian manner. Also, a conservation equation (in the Eulerian frame) is considered for the vapor mass fraction. For simplicity, the vapor is assumed to have the same properties as those of the gas. In this manner, the gas–vapor mixture (hereinafter also referred to as the carrier phase or the fluid) is treated as one entity—the Eulerian continuity, momentum, and energy equations are solved for the gas–vapor mixture. The specific enthalpy of the vapor, however, is considered to be different than that of the gas in order to satisfy the first law of thermodynamics.

2.1. *Gas–vapor equations*

The carrier phase (composed of the gas and the vapor) is considered to be a compressible and Newtonian fluid with zero bulk viscosity, and to obey the perfect gas equation of state. The Eulerian forms of the non-dimensional continuity, momentum, and energy equations for the carrier phase are, respectively, expressed as:

$$\frac{\partial \rho}{\partial t} + \frac{\partial}{\partial x_j}(\rho u_j) = \mathscr{S}_m \tag{1}$$

$$\frac{\partial}{\partial t}(\rho u_i) + \frac{\partial}{\partial x_j}(\rho u_i u_j) = -\frac{\partial p}{\partial x_i} + \frac{2}{Re_f}\frac{\partial}{\partial x_j}\left(S_{ij} - \frac{1}{3}\Delta\delta_{ij}\right) + \rho\mathscr{F}_i + \mathscr{S}_{ui} \tag{2}$$

$$\frac{\partial E_T}{\partial t} + \frac{\partial}{\partial x_j}[u_j(E_T + p)] = \frac{1}{(\gamma-1)Re_f Pr M_f^2}\frac{\partial^2 T}{\partial x_j \partial x_j} + \frac{2}{Re_f}\frac{\partial}{\partial x_j}\left[u_i\left(S_{ij} - \frac{1}{3}\Delta\delta_{ij}\right)\right] + \rho u_i \mathscr{F}_i + \mathscr{S}_e \tag{3}$$

and the conservation equation for the vapor mass fraction is described as:

$$\frac{\partial}{\partial t}(\rho Y) + \frac{\partial}{\partial x_j}(\rho Y u_j) = \frac{1}{Re_f Sc}\frac{\partial^2 Y}{\partial x_j \partial x_j} + \mathscr{S}_m. \tag{4}$$

The equation of state is $p = \rho T/\gamma M_f^2$. All of the variables are normalized by reference length, density, velocity, and temperature scales. The coupling of the carrier phase with the droplets is through the terms $\mathscr{S}_m$, $\mathscr{S}_{ui}$, and $\mathscr{S}_e$ which describe the mass, momentum, and energy exchange between the phases, respectively. The formulation of these terms and their calculation from the discrete droplet fields are described in Section 2.2.

With the knowledge of the velocity field, the solution of equation (3) provides the internal energy of the mixture of the gas and the vapor. The vapor mass fraction is then used to determine the temperature of the mixture by using relations $h_g = T$ and $h_v = T + \lambda$ for the enthalpies of the gas and the vapor, respectively. Here, the enthalpies are nondimensionalized by $C_p T_f$ and it is assumed that the specific heat of the liquid is the same as that of the gas. With the ideal gas assumption for both the gas and the vapor, the change in the enthalpy upon mixing is negligible and the enthalpy of the mixture can be described as the mass-weighted sum of the enthalpies of its constituents. After some algebraic manipulations the following relation is obtained for the internal energy of the gas–vapor mixture:

$$E_I = \frac{\rho T + \rho\gamma\lambda Y}{\gamma(\gamma-1)M_f^2} \tag{5}$$

which yields:

$$T = \frac{\gamma(\gamma-1)M_f^2 E_I}{\rho} - \gamma\lambda Y. \tag{6}$$

2.2. *Droplet equations and coupling terms*

The liquid droplets are allowed to evaporate and are assumed to remain spherical with diameter smaller than the smallest length scale of the turbulence and to exhibit an empirically corrected Stokesian drag force. Both interior motions and rotation of the droplets are neglected. The density of the droplets is considered to be constant and much larger than the density of the carrier phase such that only the inertia and the drag forces are significant to the droplet dynamics. The volume fractions considered here, are in the order of 10^{-3}. Recent studies (e.g. Laviéville *et al.* [9]) indicate that (in case of solid particles) for volume fractions of this order inter-particle collisions do not significantly modify the two-phase flow; thus the effects of the droplet collisions are not considered. The radiation heat transfer is also neglected as the temperature variations are not very large. The droplets are tracked individually in a Lagrangian manner, and the droplet position, velocity, temperature, and mass are determined from the following non-dimensional equations [10]:

$$\frac{dX_i}{dt} = v_i \tag{7}$$

$$\frac{dv_i}{dt} = \frac{f_1}{\tau_d}(u_i^* - v_i) \tag{8}$$

$$\frac{dT_d}{dt} = \frac{f_2}{\tau_d}(T^* - T_d) - \frac{f_3}{\tau_d}(Y_s - Y^*) \tag{9}$$

and

$$\frac{dm_d}{dt} = -f_4 \tau_d^{1/2}(Y_s - Y^*). \tag{10}$$

The non-dimensional droplet time constant, for Stokesian drag of a sphere, is $\tau_d = Re_f \rho_d d_d^2/18$. The droplet variables are normalized using the same reference scales as those used for the gas phase variables. The function $f_1 = (1 + 0.15\,Re_d^{0.687})/(1+B)$ in equation (8) represents an empirical correction to the Stokes drag due to droplet Reynolds numbers of order unity and larger and is valid for droplet Reynolds numbers $Re_d \leqslant 1000$ [11]. The factor involving B is

due to the effects of evaporation on drag; for non-evaporating droplets $B \equiv 0$.

The droplets are assumed 'lumped', so that there is no temperature variation within each droplet. The factor $f_2 = (Nu/3\,Pr)$ in equation (9) represents a correlation for the convective heat transfer coefficient based on an empirically corrected Nusselt number $[Nu = (2+0.6\,Re_d^{0.5}\,Pr^{0.33})/(1+B)]$ [12]. The second term on the right hand side (RHS) of equation (9) represents the change of the thermal energy due to phase change. The correlation $f_3 = (\rho^* Sh\lambda/3\,Sc)$ is a function of an empirically corrected Sherwood number, $Sh = 2+0.6Re_d^{0.5}\,Sc^{0.33}$, [12]. The vapor mass fraction at the droplet surface is equal to the vaporization pressure of the droplet (for equivalent molecular weights of the gas and the liquid) and obeys the Clausius–Clapeyron equation:

$$Y_s = P_{vap} = \exp\left[\frac{\gamma\lambda}{(\gamma-1)T_B}\left(1-\frac{T_B}{T_d}\right)\right] \quad (11)$$

where the boiling temperature of the liquid is assumed to be constant. Finally, equation (10) governs the rate of mass transfer from the droplet due to phase change which is a function of the vapor mass fraction difference at the droplet surface, the droplet time constant, and the Sherwood number dependent correlation, $f_4 = \pi(18/\rho_d)^{0.5}(\rho^* Sh/Re_f^{1.5}\,Sc)$.

The source/sink terms $\mathscr{S}_m$, $\mathscr{S}_{ui}$, and $\mathscr{S}_e$ appearing in equations (1)–(4) represent the integrated effects of the droplet mass, momentum, and energy exchange with the carrier phase. These Eulerian variables are calculated from the Lagrangian droplet variables by volume averaging the contributions from all of the individual droplets residing within the cell volume centered around each grid point. The coupling terms are expressed as:

$$\mathscr{S}_m = -\frac{1}{\delta\mathscr{V}}\sum^{n_d}\frac{dm_d}{dt} \quad (12)$$

$$\mathscr{S}_{ui} = -\frac{1}{\delta\mathscr{V}}\sum^{n_d}\frac{d}{dt}(m_d v_i) \quad (13)$$

$$\mathscr{S}_e = -\frac{1}{\delta\mathscr{V}}\sum^{n_d}\left[\frac{1}{(\gamma-1)M_f^2}\frac{d}{dt}(m_d T_d) + \frac{d}{dt}\left(\frac{1}{2}m_d v_i v_i\right)\right]. \quad (14)$$

Equation (12) simply translates the evaporated mass of the droplets to a source term for the carrier phase continuity and the vapor mass fraction equations. The momentum source term given in equation (13) may be described as the sum of two terms: $-(1/\delta\mathscr{V})\,\Sigma^{n_d} m_d(dv_i/dt)$ and $-(1/\delta\mathscr{V})\,\Sigma^{n_d}(dm_d/dt)v_i$; the first is the momentum transfer due to drag while the second represents the momentum carried to the carrier phase by the evaporated mass. The first term on the RHS of equation (14) is due to the change in the internal energy of the droplets. By manipulating equations (9) and (10), it is easy to show that $d(m_d T_d)/dt$ represents the exchange of the internal energy by convective heat transfer in addition to the internal energy carried to the carrier phase by the vapor. The last term on the RHS of equation (14) is due to the change in the kinetic energy of the droplets.

The source/sink terms described by equations (12)–(14) reduce to those for solid particles by simply inserting $dm_d/dt = 0$. The equations presented in this section for the Eulerian–Lagrangian system are in agreement with the analogous equations presented in the Eulerian–Eulerian framework by Jackson and Davidson [13].

2.3. *Numerical considerations*

Simulations are conducted within the domain $0 \leqslant x_i \leqslant 2\pi$. A Fourier pseudospectral [14] method with triply periodic boundary conditions is employed for the spatial representation of the carrier phase variables and the vapor mass fraction. All calculations are performed in Fourier space with the exception of the nonlinear terms. Aliasing errors are treated by truncating energies outside of a spherical wavenumber shell having radius $\sqrt{2}N/3$ (where N is the number of grid points in any direction) and time advancement is performed using an explicit second order accurate Adams–Bashforth method. To emulate the stationary isotropic turbulence field, a low wavenumber solenoidal forcing scheme is imposed. This is implemented by adding energy to the large scales of the turbulence at a statistically constant rate [15].

Once the carrier phase is simulated, the Lagrangian droplet equations are advanced in time using the second order accurate Adams–Bashforth method. In order to evaluate the carrier phase variables at the droplet location a fourth order accurate Lagrange polynomial interpolation scheme is employed. The accuracy of the interpolation scheme has been tested via comparisons made with the exact values calculated using the full spectral description [16]. Periodic boundary conditions are applied to the dispersed phase; when a droplet leaves the domain from one side, it is returned to the box from the opposite side. Once the droplet time constant reaches below 0.1 the droplet is removed from the simulation to avoid excessive computational requirements for tracking very small droplets; no droplet is substituted for the removed droplet. The total number of remaining droplets, however, is monitored to ensure that the Lagrangian statistics are accurate. For all of the cases considered in this study, the total number of droplets used for Lagrangian statistics is always larger than 1.2×10^5. Following Yeung and Pope [17], the statistical sampling error decreases as $N_d^{0.5}$; using 1.2×10^5 droplets results in less than 0.3% error.

The reference length is conveniently chosen such that the normalized length of the computational box is 2π. The reference temperature and density are the initial mean temperature and mean density of the carrier phase, respectively. The reference Mach number

Table 1. Cases considered in DNS. All of the cases are with two-way coupling

Case	τ_{d0}	ϕ_{m0}	T_{d0}	T_B	Y_0	λ	Evaporation	N_d	τ_{d0}/τ_k
C1	2.5	0.25	1	2	0	0.8	Yes	138713	0.73
C2	2.5	0.5	1	2	0	0.8	Yes	277426	0.68
C3	2.5	1	1	2	0	0.8	Yes	554852	0.62
C4	6.25	1	1	2	0	0.8	Yes	140368	1.41
C5	2.5	0.25	0.2	2	0	0.8	Yes	138713	0.73
C6	2.5	0.5	0.2	2	0	0.8	Yes	277426	0.68
C7	2.5	1	0.2	2	0	0.8	Yes	554852	0.62
C8	6.25	1	0.2	2	0	0.8	Yes	140368	1.41
C9	2.5	0.5	1	5	0	0.8	Yes	277426	0.68
C10	2.5	0.5	1	2	0.2	0.8	Yes	277426	0.68
C11	2.5	0.5	1	2	0	2	Yes	277426	0.68
C12	2.5	0.5	1	—	0	—	No	277426	0.68

is $M_f = 1$; therefore, the speed of sound based on the initial mean gas temperature is the reference scale for the velocity. For all the simulations, $Re_f = 500$, $Pr = Sc = 0.7$, $\Gamma = 1.4$, and $\rho_d = 1000$. Direct numerical simulations are performed employing 64^3 collocation points for the carrier phase and as many as 5.5×10^5 droplets for the dispersed phase. In order to generate stationary initial conditions, the droplets are allowed to interact with the flow (as solid particles) for more than three eddy-turn-over times. Once all of the statistics reach stationary state, the time is set to zero and simulations of the evaporating droplets begin. A typical run for the case with the highest number of droplets has taken about 60 h of CPU time on a CRAY C90 supercomputer. The mean Mach number is less than 0.2 for all of the cases and the flow is free of shock, therefore, 64^3 collocation points suffice to accurately resolve the flow field. An indicative of the resolution is the value of ηk_{max} (η and k_{max} are the Kolmogorov length scale and the highest wave number resolved, respectively) which has been greater than two for all of the simulations. The time averaged (over a sufficiently long interval in the stationary, nonevaporating part of the simulations) values of the Taylor microscale Reynolds number and the eddy-turn-over time for various cases vary between 25 and 35, and between 3.03 and 4.05, respectively.

3. RESULTS

An inspection of the formulation in Section 2 identifies the significant parameters as: the initial droplet time constant (τ_{d0}), the initial mass loading ratio (ϕ_{m0}), the initial droplet temperature (T_{d0}), the normalized droplet heat of evaporation (λ), the boiling temperature (T_B), and the initial vapor mass fraction (Y_0, which is considered to be spatially uniform). Table 1 provides a listing of the cases considered to study the effects of these parameters. Due to the large number of parameters involved in the problem, a detailed parametric study is not possible. Therefore, we perform a case study in order to compare the effects of the variation of each parameter. Case C1–C4 are to study the effects of the mass loading ratio and the droplet time constant while initially droplets have the same temperature as that of the carrier phase, i.e. $T_{d0} = 1$. Cases C5–C8 are analogous to C1–C4, but with $T_{d0} = 0.2$, in order to study the effects of the initial droplet temperature. The effects of the parameters that more directly influence the evaporation process (i.e. T_B, Y_0 and λ), are investigated by considering cases C9–C11. Finally, case C12 without evaporation, is considered to assess the effects of evaporation via comparison with the analogous evaporating case C3. In all of the cases a full two-way coupling between the droplets and the carrier phase is considered. The case with $Y_0 = 0.2$ is initialized in such a way that the initial carrier phase mean density remains the same as in other cases (i.e. $\langle \rho \rangle = 1$ at $t = 0$); the mean density of the gas alone is 0.8 for this case. The values of τ_{d0}/τ_k (calculated at $t = 0$) in Table 1 are useful in identifying the scales of the flow which are more effectively interacting with the droplets.

The extensive data generated by DNS may be used to investigate the effects of the above parameters on various statistics of the carrier and the dispersed phases. In this paper, however, we focus our attention on some of the issues which are of more interest in spray modeling, namely the droplet size, the temperature, and the vapor mass fraction. The analysis of DNS results indicates that the amount of energy added to the system by external forcing is very negligible in comparison to phase change energy. Therefore, the statistics presented here are not affected by external forcing.

3.1. *Droplet size*

In Fig. 1 results are presented of the temporal variations of the Lagrangian-averaged values of the square of the droplet diameter $\langle\langle d_d^2 \rangle\rangle$ as normalized with its initial value. The nonlinear variations of $\langle\langle d_d^2 \rangle\rangle$ during the early times as portrayed in this figure are not in accord with the d^2-law [18] which is commonly used for modeling of evaporation of a single droplet. At long times, however, the rate of

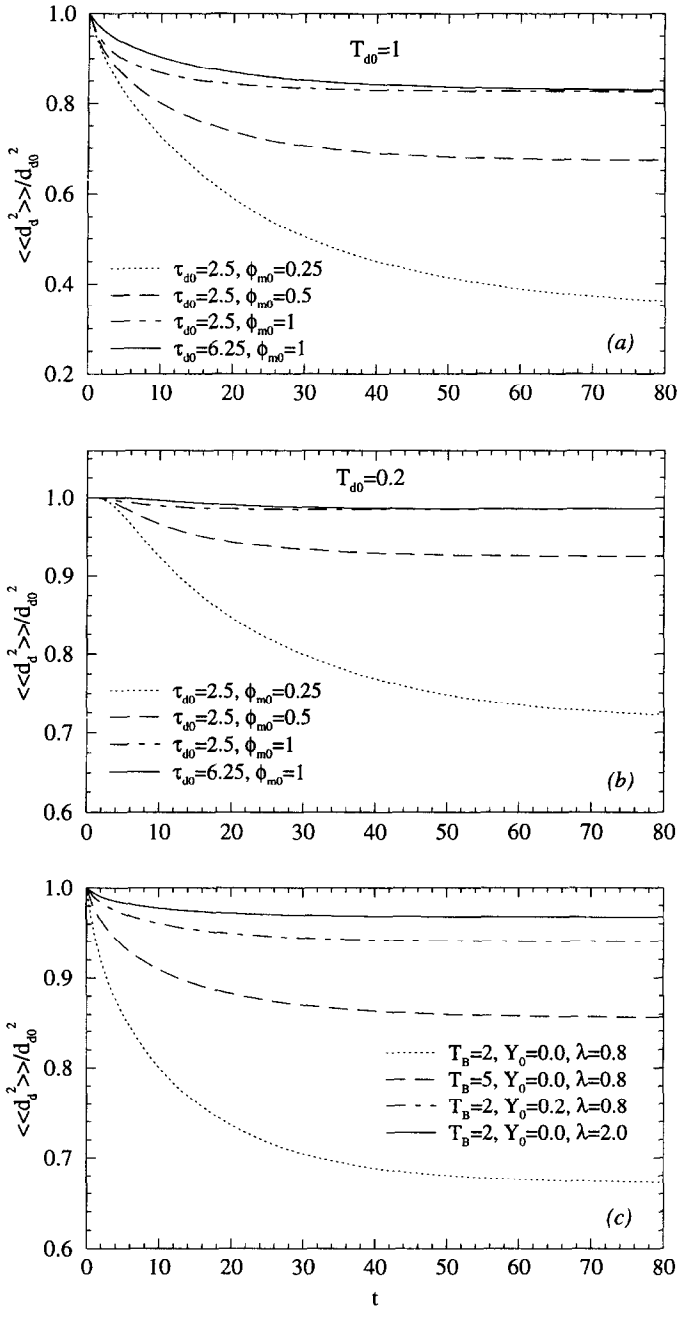

Fig. 1. The mean droplet diameter-squared normalized with its initial value. (a) Cases C1–C4, (b) cases C5–C8, and (c) cases C3, and C9–C11.

evaporation approaches asymptotic values which may be comparable to those predicted by the d^2-law. It is shown that with the increase of the mass loading ratio, the temporal variation of $\langle\langle d_d^2\rangle\rangle$ becomes more nonlinear during the early times, and the rate of evaporation decreases. It is also shown that larger particles have smaller values for $\langle\langle d_d^2\rangle\rangle/d_{d0}^2$. The effect of the decrease of the initial droplet temperature on droplets sizes is realized via comparison of Fig. 1(b) with Fig. 1(a). Similar trends for the variations of $\langle\langle d_d^2\rangle\rangle$ with the mass loading ratio and the droplet time constant are observed, however, the evaporation rate is significantly decreased by the decrease of the initial droplet temperature. This is in accord with physical intuition and is due to the decrease of the vapor mass fraction on the surface of the droplet as is evident from equation (10). The decrease in the evaporation rate is more visible during the early stages of evaporation ($t < 3$). During this period the heat transfer from the carrier phase is mostly consumed to increase

the droplets temperature. Figure 1(c) indicates that the increase of the boiling temperature, the initial vapor mass fraction or the latent heat of evaporation results in the decrease of the evaporation rate.

The general trends observed in Fig. 1 can be explained by analyzing the variation of the evaporated mass of the droplets. Figure 1(a) indicates that the increase of the mass loading ratio decreases the evaporated mass (relative to the initial mass) of the droplets. This is due to the increase of the vapor mass fraction as the absolute evaporated mass increases with the increase of the mass loading ratio. Consequently, the difference $Y_s - Y^*$ which determines the rate of evaporation, decreases and the individual droplets evaporate with smaller rates. Figure 1(a) also shows that for the same mass loading ratio, the increase of the droplet time constant results in the decrease of the evaporated mass. Equation (10) indicates that the rate of change of d_d^2/d_{d0}^2 is inversely proportional to d_{d0}^2. Therefore, with the increase of τ_d, the evaporation rate decreases and so does the evaporated mass of the droplets. The physical explanation is that smaller droplets have a larger surface to volume ratio as compared to larger droplets. Since the evaporated mass is proportional to the surface area, the smaller droplets evaporate more mass per unit volume. The increase of T_B results in the decrease of Y_s [equation (11)] and thus the decrease of the evaporation rate as indicated by equation (10). This equation also indicates that by increasing the initial vapor mass fraction, the rate of evaporation decreases. The increase in λ can be interpreted as the increase of the droplet latent heat of evaporation which delays the evaporation process. This is also evident from equation (11) which indicates a decrease in Y_s, and, therefore, the evaporation rate, with the increase of λ.

The polydispersity due to droplets' evaporation is examined by considering the distribution of the droplet sizes. The skewness and kurtosis of the droplet diameter as shown in Fig. 2 provide a quantitative means of assessing this distribution. The profiles of the probability density functions (pdfs) are also monitored at all times, but are not presented here. It appears that both the skewness and the kurtosis approach asymptotic values at long times. The asymptotic skewness is negative for all of the cases, indicating that the pdfs are skewed towards smaller droplet sizes. Figure 2(a), for large initial droplet temperature, indicates that at small mass loading ratios the pdf of the droplet size is approximately, Gaussian. But the pdfs deviate more from Gaussian as the mass loading ratio increases. It is also noted that the increase of the droplet time constant results in pdfs closer to Gaussian. Examinations of all the cases indicate that ϕ_{m0} is more influential on the pdf than are all the other parameters. For small values of the mass loading ratio, the results are in qualitative agreement with those via one-way coupling in incompressible flows [8] and confirm the important role of the mass loading on the droplet size distribution. Comparisons of the long time values of the skewness in Fig. 2(a) and (b) indicate that the pdf is more influenced (by the decrease of the initial droplet temperature) in the case with the smallest mass loading ratio.

3.2. *Temperature*

The temporal variations of the mean temperature are shown in Fig. 3 for both phases with $T_{d0} = 1$. For all of the cases, a sharp decrease in the droplet mean temperature is observed during the early stages of evaporation. This is due to the initial large difference between the vapor mass fraction at the surface of the droplet (Y_s) and that in the surrounding carrier phase (Y^*). This difference is positive during the early times and, as equation (9) indicates, tends to decrease the droplet internal energy. The physical interpretation is that initially the droplets are not in equilibrium with the vapor in their surrounding carrier phase, and a large gradient exists for the vapor concentration around each droplet. This causes the droplets to evaporate with high rates. Since the temperature difference between the two phases is small during this initial period the convective heat transfer from the carrier phase to the droplets is not very effective and the energy required for phase change must be provided by decreasing the internal energy of the droplets. Once the temperature difference is increased the evaporation process is sustained by heat transfer from the carrier phase. In the meantime, evaporation decreases the difference between the vapor mass fraction at the surface of the droplet and that in the carrier phase. Therefore, while in the beginning evaporation is mainly due to the vapor concentration gradient, at long times it is more supported by heat transfer from the carrier phase.

An interesting feature is associated with the mass loading ratio in Fig. 3(a). By increasing this ratio, the mean temperature of the carrier phase decreases in early stages of evaporation, while during intermediate and long times an opposite trend is observed. During short times, the increase of the mass loading ratio increases the evaporated mass (see Fig. 1(a)) and results in the monotonic decrease of the mean carrier phase temperature. At longer times, Fig. 1(a) indicates that the rate of mass evaporation approaches small values. Therefore, the evaporation mechanism for decreasing the mean carrier phase temperature becomes somewhat ineffective at long times. On the other hand, the droplet temperature decays faster than the carrier phase temperature during the initial times, resulting in the increase of the temperature difference between the two phases. An inspection of Fig. 3(a) and (c) reveals that the temperature difference between the two phases is larger for smaller mass loading ratios. Therefore, the convection mechanism becomes effective for small mass loading ratios, resulting in the decrease of the temperature of the carrier phase. The increase of the initial droplet time constant, at the same initial mass loading ratio, results in higher mean

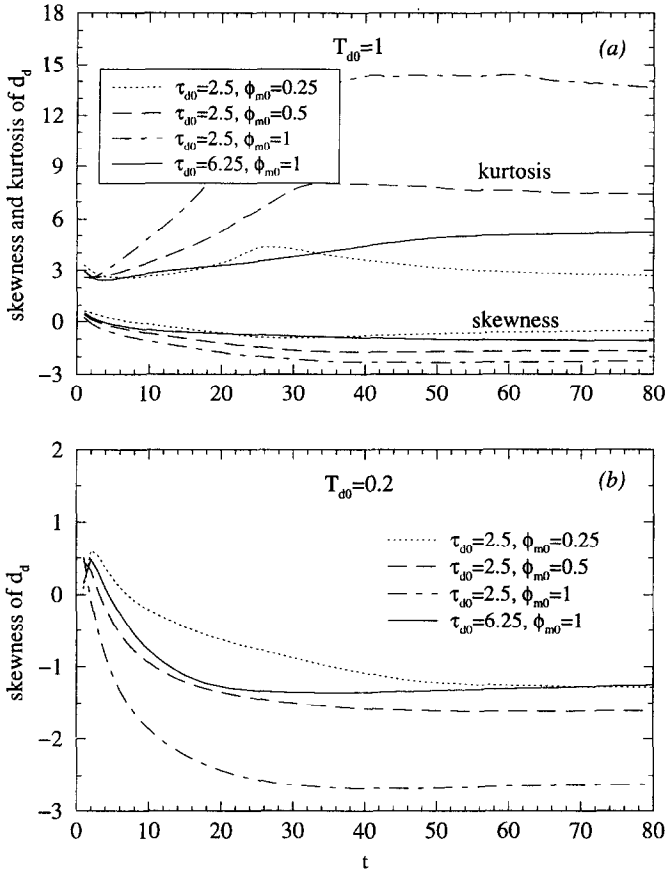

Fig. 2. Variations of (a) the skewness and the kurtosis of the droplet diameter for cases C1–C4, and (b) the skewness of the droplet diameter for cases C5–C8.

droplet temperature as the larger droplets have larger heat capacity (the product of the mass of the droplet and its specific heat). The variation in the mean temperature of the carrier phase with the increase of the droplet time constant, however, is not monotonic. During the early times, the evaporation rate is smaller for larger droplets, thus, the mean carrier phase temperature increases with the increase of the droplet time constant. This, however, results in a larger temperature difference between the phases for larger droplets. Therefore, at long times the heat transfer between the larger droplets and the carrier phase is higher and the temperature of the carrier phase decreases below its level in the case with smaller droplets. The increase of T_B, Y_0, or λ results in higher mean temperatures for both phases. This is mainly due to the decrease of the evaporation rate as discussed in Section 3.1.

The effects of the decrease of the initial droplet temperature on the mean temperatures of both phases is realized by the comparison of the results shown in Fig. 4(a) with those in Fig. 3(a) and (c). As expected, the mean temperatures of both phases are significantly decreased with the decrease of T_{d0}. It is noted that the trend of variation of the mean droplet temperature with the increase of the mass loading ratio is the opposite of what was observed in cases with $T_{d0} = 1$—the mean droplet temperature decreases with the increase of the mass loading ratio for cases with $T_{d0} = 0.2$. This is due to the fact that when the mass loading ratio is smaller less heat transfer from the carrier phase is required to raise the droplet temperature. Therefore, the mean temperature of the carrier phase is higher for cases with the smaller mass loading ratio, and so is the mean droplet temperature. It is also noted in Fig. 4(a) that at long times the temperatures of both phases approach asymptotic values for all of the cases. A measure of the convective heat transfer between the phases is the mean temperature difference which is depicted in Fig. 4(b). It is observed that the mean temperature difference decreases to small values within a short time after the evaporation begins. The rate of decrease is higher for larger mass loading ratios. The increase of the droplet time constant results in higher values for the mean temperature difference, again due to the larger heat capacity of larger droplets.

From a modeling standpoint, the root mean square (rms) of the fluctuating temperature of both the carrier and the dispersed phases are of great interest as the knowledge of these quantities suffices to determine

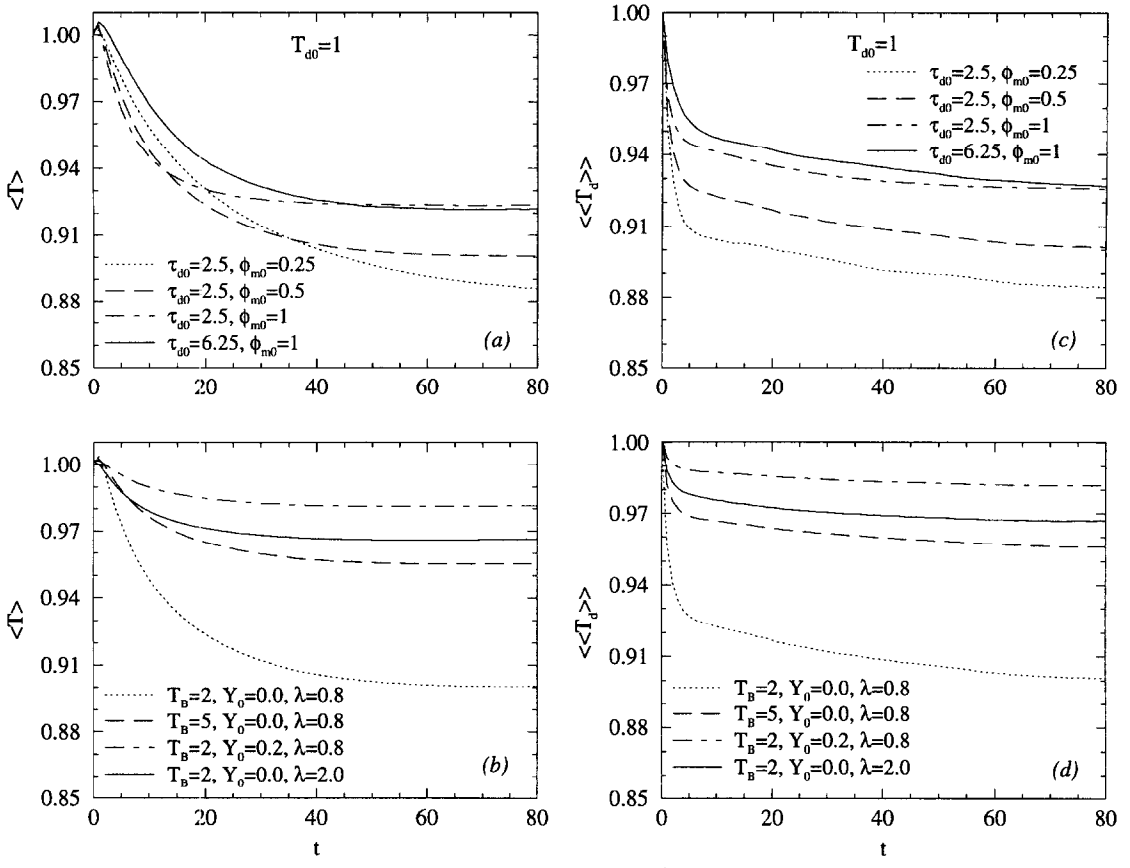

Fig. 3. Variations of the mean temperature of (a) the carrier phase, cases C1–C4, (b) the carrier phase, cases C3, and C9–C11, (c) the dispersed phase, cases C1–C4, and (d) the dispersed phase, cases C3, and C9–C11.

the mean values of the temperature. The temporal variation of $T_{\mathrm{drms}} = \sqrt{\langle\langle(T_{\mathrm{d}} - \langle\langle T_{\mathrm{d}}\rangle\rangle)^2\rangle\rangle}$ is shown in Fig. 5 for both initial droplet temperatures. The rms of the fluctuating droplet temperature obtained from the case without evaporation is also shown in Fig. 5(a) for comparison. It is observed that evaporation significantly increases the temperature fluctuations. All of the cases exhibit a peak value for T_{drms} during the early stages of evaporation, followed by a monotonic decrease. The peak values occur faster for cases with smaller initial droplet temperature. A comparison of Fig. 5(b) with Fig. 4(b) reveals that the peaks in the variations of T_{drms} correspond to the times that the mean temperature difference reaches small values. During the early times the rate of heat transfer between the two phases is large. This results in large variations in the temperatures of the droplets residing in various regions of the flow, thus increasing the temperature fluctuations. The comparison of Fig. 5(a) and (b) indicates that while the trend of variations of T_{drms} with the increase of the mass loading ratio is the same for both initial droplet temperatures before the peak time, opposite trends are observed after the peak time. It is also noted that the increase of the droplet time constant delays the peak time for cases with large initial droplet temperature. For the case with the small initial droplet temperature, the increase of the droplet time constant results in a flattening of the peak region.

3.3. *Vapor mass fraction*

The temporal variations of the mean vapor mass fraction are presented in Fig. 6. The variations of this quantity is closely related to the variations of the evaporation rate. The figure indicates that for $\tau_{\mathrm{d0}} = 2.5$, the mean vapor mass fraction approaches asymptotic values for all the mass loading ratios. The reason for this behavior is that the mixture becomes saturated at long times. This may be verified by using the long time values of the mean temperature of the dispersed phase (from Fig. 3(c)) in equation (11). For instance, for the case with $\tau_{\mathrm{d0}} = 2.5$ and $\phi_{\mathrm{m0}} = 1$, equation (11) yields $Y_{\mathrm{s}} \approx 0.195$ which is very close to the asymptotic value of $\langle Y\rangle$ portrayed in Fig. 6(a). An examination of Fig. 6(b) also indicates that $\langle Y\rangle$ reaches asymptotic values for all of the cases. This is again due to the fact that the vapor mass fraction in the carrier phase reaches its saturation value. In general, the results in Fig. 6 show that the boiling temperature, the latent heat of evaporation, and the

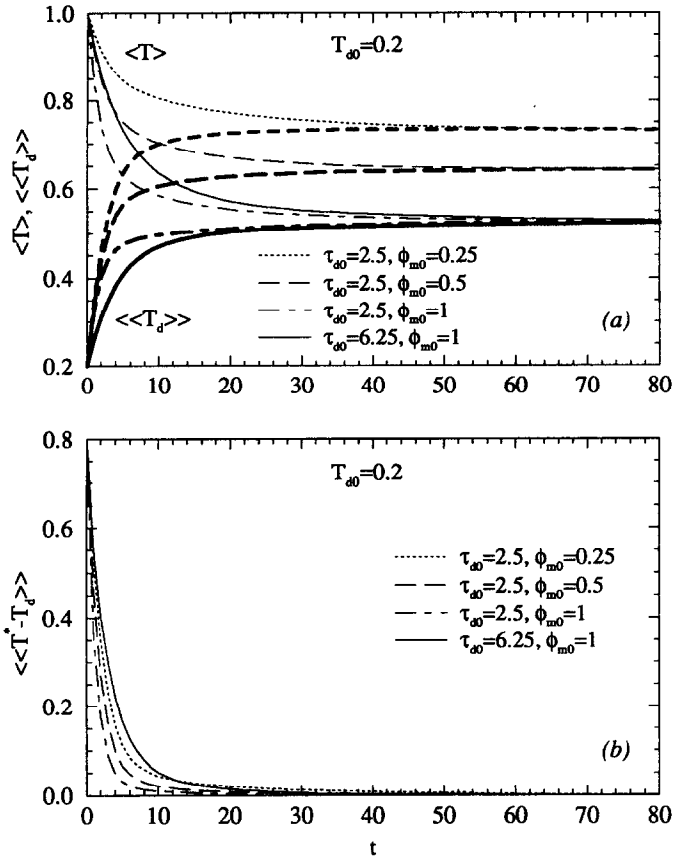

Fig. 4. Variations of (a) the mean temperatures of both phases and (b) the mean temperature difference for cases C5–C8.

initial vapor mass fraction are very influential on the amount of evaporated mass.

The temporal variations of the rms of the vapor mass fraction [$Y_{rms} = \sqrt{\langle (Y - \langle Y \rangle)^2 \rangle}$] are shown in Fig. 7. This quantity is of great interest in the modeling of the mean vapor mass fraction. For all of the cases, Y_{rms} starts from zero as the vapor mass fraction has a uniform distribution at $t = 0$. Shortly after the onset of evaporation ($t < 8$), the rms of the vapor mass fraction increases to peak values. This is due to localized production of the vapor at the droplets locations that results in a wide spatial variation of Y—note that the droplets are not uniformly distributed in the flowfield due to the effects of the preferential concentration [5, 19]. Later, turbulent stirring results in a more uniform distribution of the evaporated mass. In the meantime, the production of the vapor also decreases at long times. The combined effect of these two phenomena is a significant decay in the fluctuations of the vapor mass fraction during long times. Figure 7(a) shows that the rms peak occurs faster at higher mass loading ratios. However, at longer times the vapor is distributed more uniformly, due to saturation, and Y_{rms} takes smaller values as the initial mass loading ratio is increased. The increase of the droplet size delays the occurrence of the peak and results in higher rms values at all times after the peak time. Figure 7(b) indicates that the increase of T_B, Y_0, or λ results in the decrease of Y_{rms} at all times. These trends can be explained by considering the variations of the evaporated mass shown in Fig. 1(c).

Figure 8 illustrates the temporal variations of the mean and the fluctuations of the vapor mass fraction for cases with small initial droplet temperature. Similar to the results shown in Fig. 6(a) (for $T_{d0} = 1$), Fig. 8(a) indicates that the mean vapor mass fraction approaches asymptotic values at long times. This is again due to saturation of the vapor in the carrier phase. However, it is noted that the asymptotic values in Fig. 8(a) are smaller than those in Fig. 6(a). For cases with $T_{d0} = 0.2$, the long time droplet temperature is smaller which results in smaller values of Y_s. It is interesting that, contrary to cases with $T_{d0} = 1$, when the initial droplet temperature is low the mean vapor mass fraction decreases with the increase of the mass loading ratio. This is due to the decrease of the droplet temperature with the increase of the mass loading ratio as discussed earlier in Section 3.2. The comparisons of the rms values of the vapor mass fraction for cases with large (Fig. 7(a)) and small (Fig. 8(b)) initial droplet temperatures, reveals that the peak values appear at longer times when $T_{d0} = 0.2$.

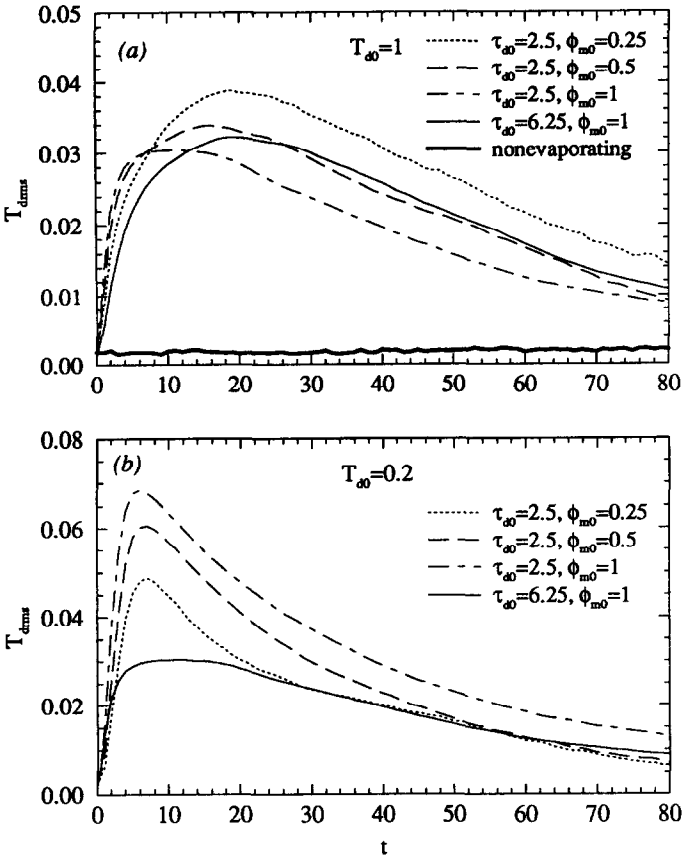

Fig. 5. The rms of the droplet temperature for (a) cases C1–C4 and C12, and (b) cases C5–C8.

Also, in general, Y_{rms} values are smaller when the initial droplet temperatures is low. This is mainly due to the decrease of the production of the vapor with the decrease of T_{d0}.

Due to its importance in the prediction of combustion process, of great interest is the behavior of the pdf of the vapor mass fraction. To analyze the pdf, the temporal variations of the skewness and the kurtosis of the fluctuating vapor mass fraction ($Y' = Y - \langle Y \rangle$) for cases with large (Fig. 9(a)) and small (Fig. 9(b)) initial droplet temperatures are considered. For cases with large initial droplet temperature, Fig. 9(a) shows that during the intermediate times, the deviation of the pdf from Gaussian increases as the mass loading ratio is increased. The increase of the droplet size, however, significantly changes the behavior of the pdf at large mass loading ratios and results in a pdf closer to Gaussian. At smaller initial droplet temperature, the pdfs are closer to Gaussian as compared to those from cases with $T_{d0} = 1$. This is particularly more visible for the case with $\tau_{d0} = 2.5$ and $\phi_{m0} = 1$. In summary (for practical purposes) the pdf of the fluctuating vapor mass fraction is reasonably approximated by a Gaussian distribution, when the initial droplet temperature is small. For large T_{d0}, a Gaussian approximation is appropriate when the droplet size is large or the mass loading ratio is small to moderate. Furthermore, for all of the cases, a Gaussian approximation seems reasonable at long times, when the mixture becomes nearly saturated.

More insight into the evolution of the fluctuations of the vapor mass fraction is obtained by considering the transport equation for the variance of this quantity. This equation is derived similarly to that for a scalar [20], and for homogeneous flows reads:

$$\frac{\partial \langle \rho Y''^2 \rangle}{\partial t} = -\varepsilon_Y + S_d \tag{15}$$

where $Y'' = Y - \tilde{Y}$ (with $\tilde{Y} = \langle \rho Y \rangle / \langle \rho \rangle$) is the Favre averaged fluctuation of the vapor mass fraction. The DNS results indicate that there is only a negligible difference between the Favre and the Reynolds averaged fluctuations of Y. In equation (15),

$$\varepsilon_Y = \frac{2}{Re_f Sc} \left\langle \frac{\partial Y''}{\partial x_i} \frac{\partial Y''}{\partial x_i} \right\rangle$$

is the dissipation rate, and S_d indicates the source term due to droplet evaporation.

The temporal variations of ε_Y and S_d are presented in Fig. 10 for various mass loading ratios. The figure

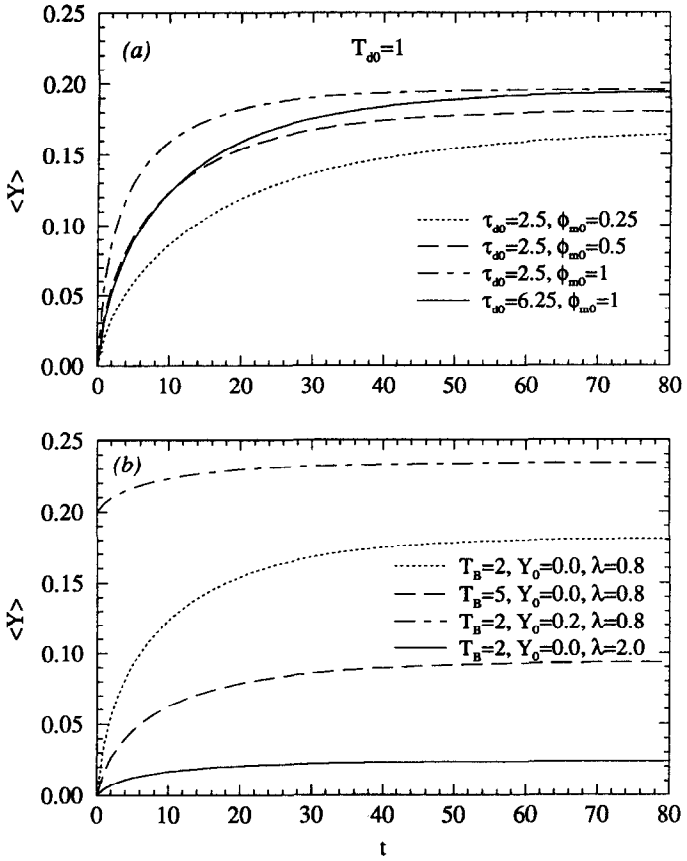

Fig. 6. The mean vapor mass fraction for (a) cases C1–C4, and (b) cases C3, and C9–C11.

indicates that, for cases with large initial droplet temperature, shortly after the onset of evaporation the dissipation reaches large values and then monotonically decreases in time. During the early stages of evaporation, ε_Y increases with the increase of the mass loading ratio while an opposite trend is observed during intermediate and long times. For cases with small initial droplet temperature, the occurrence of the peak value is delayed, and the dissipation exhibits a decreasing trend with the increase of the mass loading ratio throughout the simulation. A comparison of Figs 10(a) and (b) reveals that the short time values of the dissipation are much higher for cases with $T_{d0} = 1$; at long times, however, the dissipation is comparable for both cases with small and large initial droplet temperatures. These trends are closely related to the variations of the evaporation rate.

While the dissipation term in equation (15) tends to decrease the variance of the vapor mass fraction fluctuations, the source term due to the droplet evaporation (S_d) acts in the opposite direction as witnessed by positive values of this quantity illustrated in Figs. 10(c) and (d). This term has been calculated using equation (15). In general, similar trends with the variations of the mass loading ratio are observed as those noted for the dissipation. However, during the initial times S_d is larger than ε_Y, thus the variance of the fluctuating vapor mass fraction increases in time, in agreement to the results shown in Figs. 7(a) and 8(b). During the longer times, the rate of vapor production is significantly decreased. This results in the decrease of S_d to values smaller than ε_Y, thus the variance decays. It is noted that, during the long times, both the dissipation and the droplet source term assume very small values. As a result, the fluctuations of the vapor mass fraction approach quasistationary states, while the mean values of this quantity reach saturation levels.

Some insight into the structural evolution of the vapor mass fraction is gained by considering the evolutions of the lengthscale and the power spectra of this quantity. The temporal variations of the Taylor microscale (λ_Y) of the vapor mass fraction are shown in Fig. 11. The microscale here is defined as $\lambda_Y = \sqrt{12Y'^2/(Re_f Sc\varepsilon_Y)}$, similarly to the microscale defined for a scalar [21]. Figure 11(a) shows that, for the cases with large initial droplet temperature, the microscale reaches stationary values after a relatively short time. The stationary values appear to be rather independent of the mass loading ratio. For cases with small T_{d0}, the growth period of the microscale extends to longer times. In fact, for the case with the highest

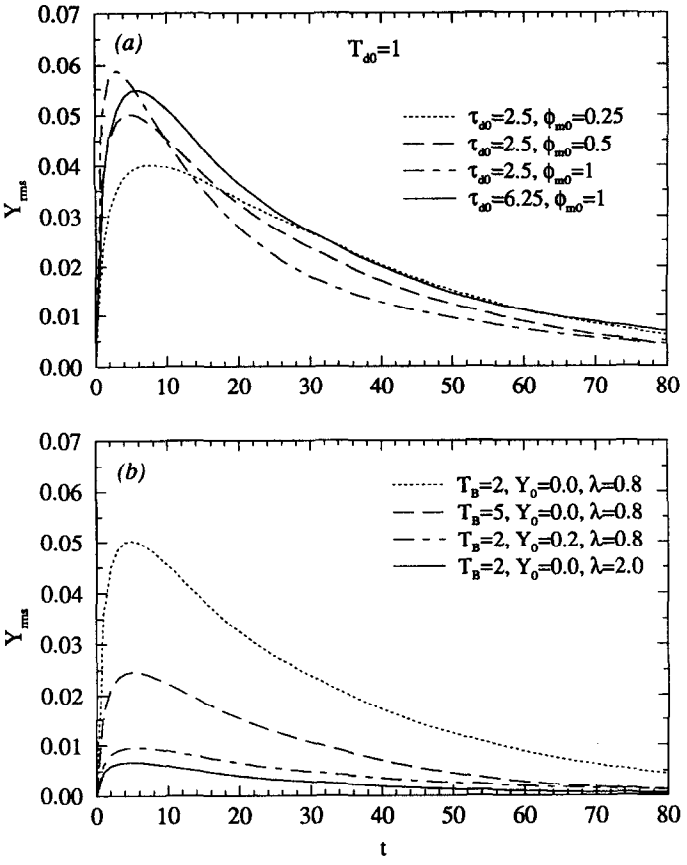

Fig. 7. The rms of the vapor mass fraction for (a) cases C1–C4, and (b) cases C3, and C9–C11.

mass loading ratio, the microscale never reaches a stationary value during the simulation time. It is also noted that λ_Y increases with the increase of the mass loading ratio when $T_{d0} = 0.2$. It is not clear, from the results of the present simulations, whether at longer times the values of λ_Y will decrease to (lower) asymptotic values observed for the cases with $T_{d0} = 1$.

The power spectra $E_Y(k)$ of the fluctuations of the vapor mass fraction are shown in Fig. 12 for the case with $\tau_{d0} = 2.5$ and $\phi_{m0} = 0.5$, for both small and large initial droplet temperatures. These spectra are normalized with the variance of the fluctuating vapor mass fraction in order to facilitate the comparisons. The figure shows that during the early stages of evaporation, the energy is more uniformly distributed among large and small scales. As the rate of production of the vapor decreases, at longer times, the spectra become self similar with much of the energy concentrated in low wavenumbers. Therefore, it seems that the production term in equation (15) contributes more to large and moderate scales. These results are in qualitative agreement with the temporal evolutions of the Taylor microscale shown in Fig. 11. The results shown in Fig. 12(b) indicate that for the case with $T_{d0} = 0.2$, the spectra do not become self similar during the simulation time. However, these results do show that most of the energy is concentrated in low wavenumbers at long times.

4. CONCLUSIONS

Direct numerical simulations have been conducted of the dispersion and polydispersity of evaporating droplets in forced turbulence at low Mach numbers. The carrier phase is simulated in Eulerian frame, the dispersed phase is tracked in a Lagrangian manner, and a (realistic) two-way coupling between the carrier and dispersed phases is considered. The DNS results are used to investigate the effects of the initial droplet time constant, the initial mass loading ratio, the initial droplet temperature, the boiling temperature, the latent heat of evaporation, and the initial vapor mass fraction on the droplet size, the temperature fields, and the vapor mass fraction.

The evaporation rate is nonlinear during the early times as the droplets are not in equilibrium with the vapor in their surrounding carrier phase. The increase of all of the above mentioned parameters, but the initial droplet temperature, results in the decrease of the evaporation rate. An opposite trend is observed with the increase of the initial droplet temperature. The pdfs of the droplet diameter are skewed towards

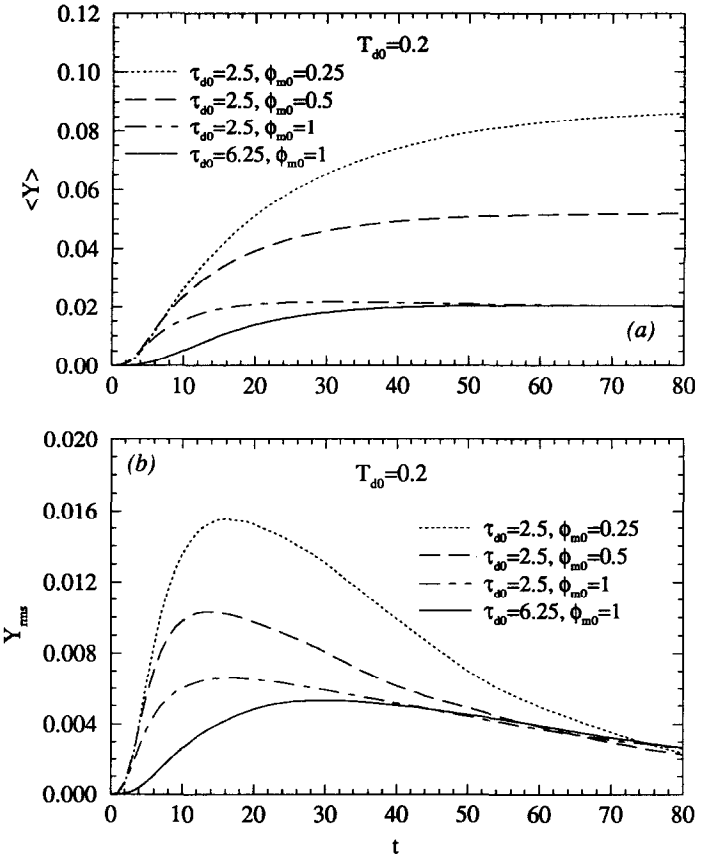

Fig. 8. Variations of (a) the mean and (b) the rms of the vapor mass fraction for cases C5–C8.

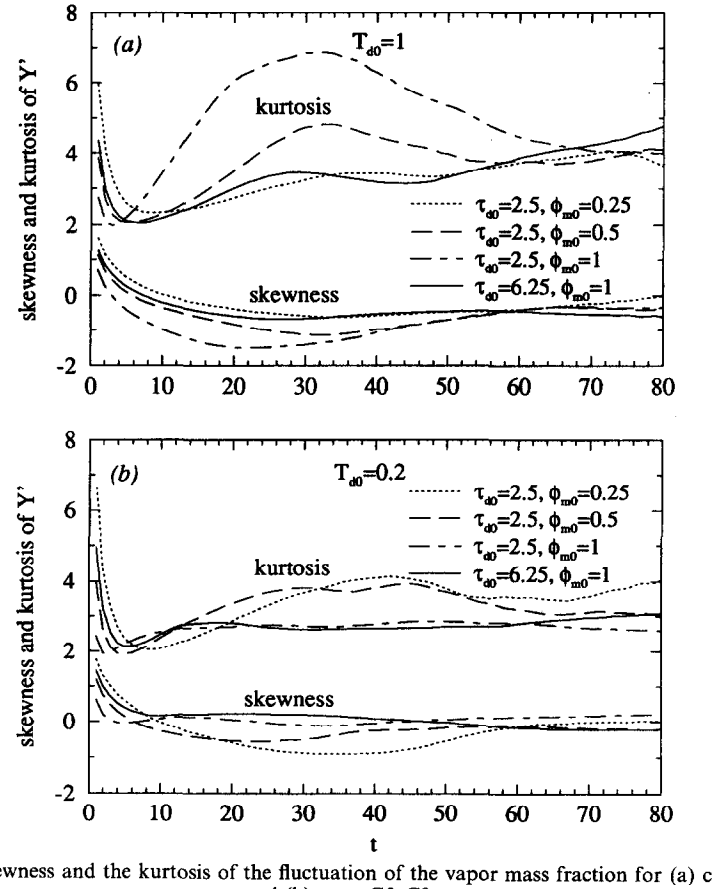

Fig. 9. The skewness and the kurtosis of the fluctuation of the vapor mass fraction for (a) cases C1–C4 and (b) cases C5–C8.

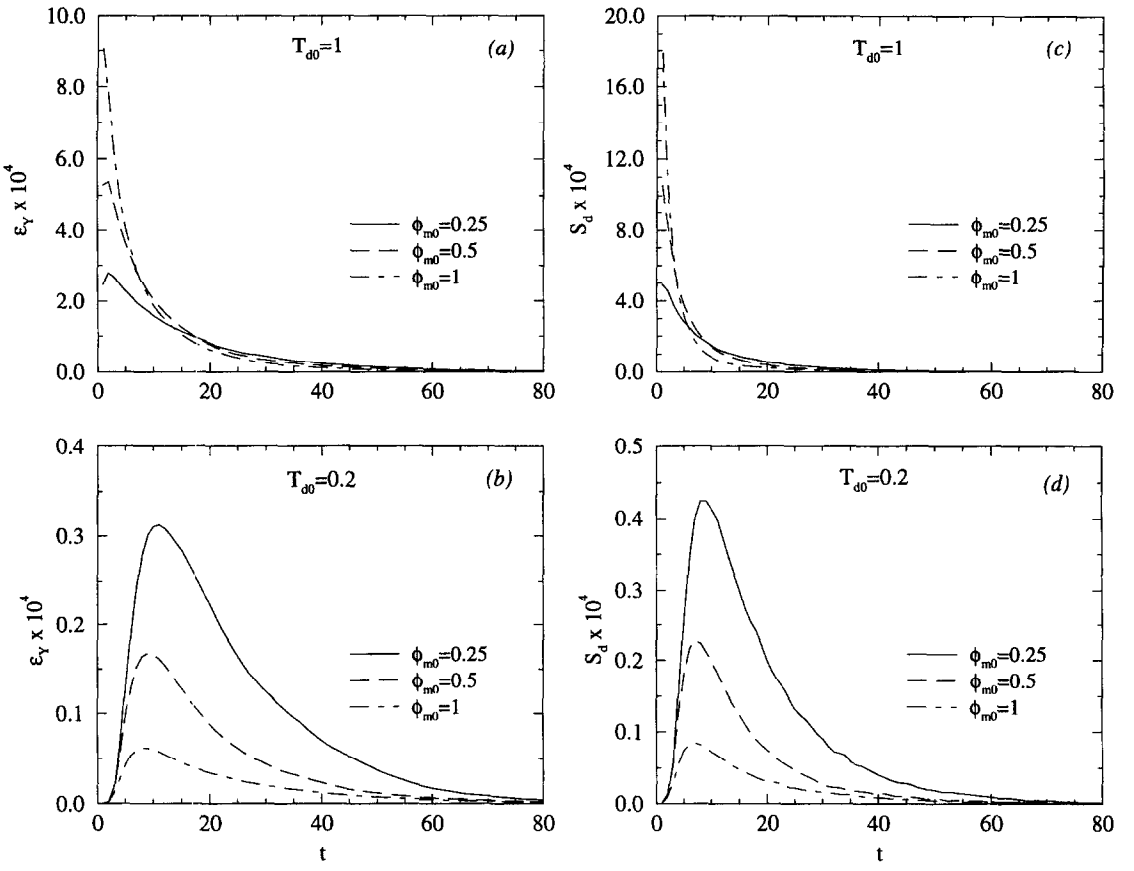

Fig. 10. Variations of the dissipation and the droplet source terms in equation (15). (a) The dissipation for cases C2–C4, (b) the dissipation for cases C6–C8, (c) the source term for cases C2–C4, and (d) the source term for cases C6–C8.

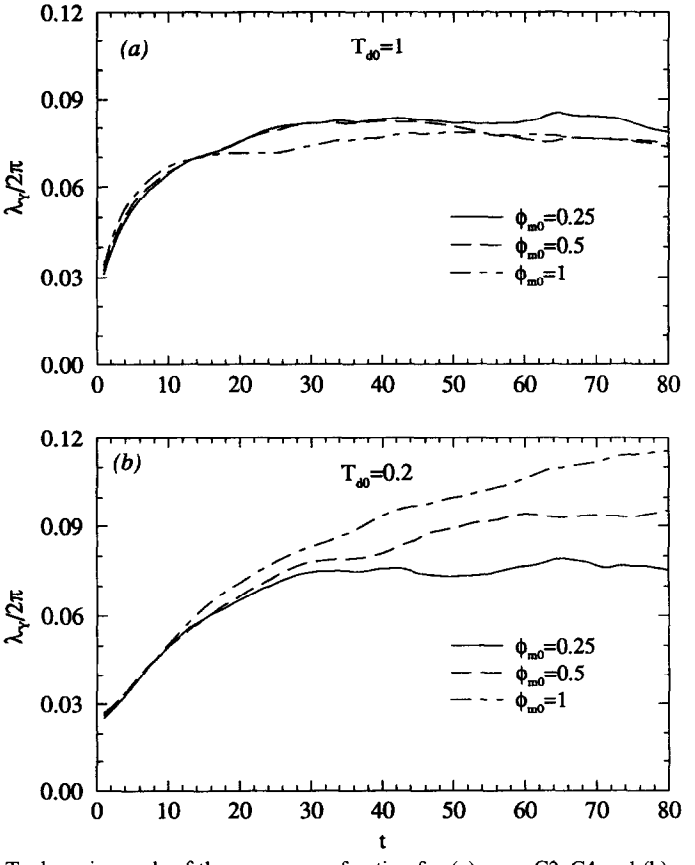

Fig. 11. The Taylor microscale of the vapor mass fraction for (a) cases C2–C4 and (b) cases C6–C8.

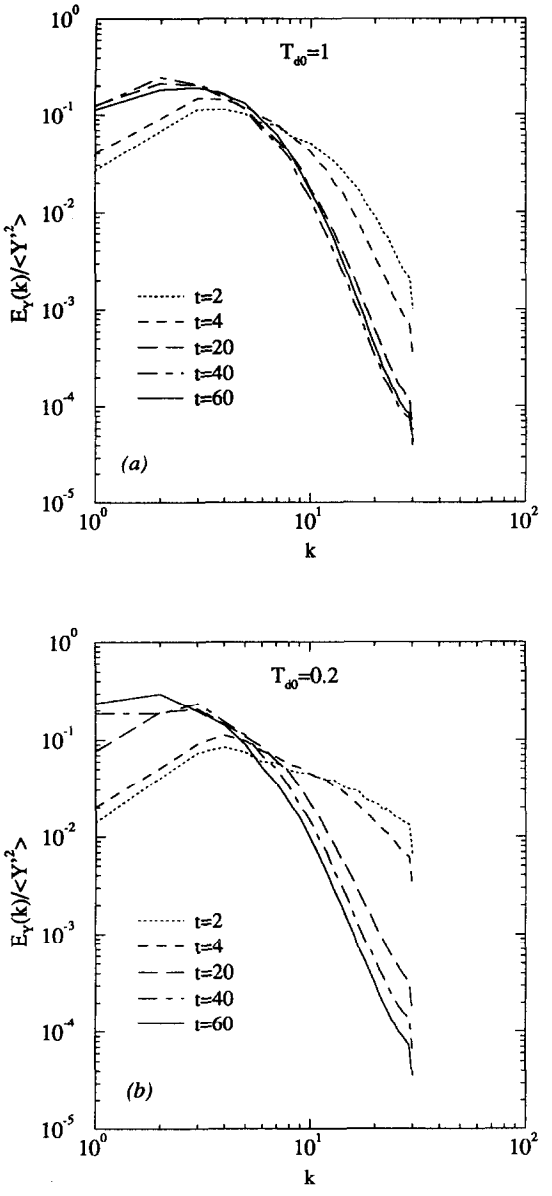

Fig. 12. Temporal evolution of the power spectra of the vapor mass fraction for (a) case C3 and (b) case C7.

smaller droplets, however, they may be approximated as Gaussian for small mass loading ratios. The mean droplet temperature exhibits a sharp decrease (increase) during the early times for cases with large (small) initial droplet temperature. For both small and large initial droplet temperatures, peak values are observed in the temporal variations of the rms of the droplet temperature fluctuations, however, the peak values occur sooner when the initial droplet temperature is smaller.

The examination of the temporal evolutions of the mean vapor mass fraction indicates that the mixture becomes nearly saturated at long times. Shortly after the onset of evaporation, the rms of the fluctuations of the vapor mass fraction reaches peak values, due to localized productions of the vapor at the droplets locations. The decrease of the initial droplet temperature delays the occurrence of the peak value in the temporal evolution of the rms fluctuating vapor mass fraction. The evolution of the fluctuating vapor mass fraction is more closely investigated by considering the transport equation for its variance. In cases with large initial droplet temperature, the Taylor microscale of the vapor mass fraction reaches stationary values which are rather independent of the mass loading ratio. In cases with small initial droplet temperature, the microscale increases with the increase of the mass loading ratio, and does not reach stationary state when the mass loading ratio is large. An analysis of the power spectra of the vapor mass fraction fluctuation indicates that during the early stages of evaporation, the energy is rather uniformly distributed among various scales. At longer times, most of the energy is concentrated at low wavenumbers and the spectra becomes self similar. The latter is only true when the initial droplet temperature is large.

Acknowledgement—Computational resources for this work were in part provided by the Pittsburgh Supercomputing Center and the College of Engineering Computer Facility at University of Hawaii at Manoa.

REFERENCES

1. Riley, J. J and Patterson, G. S., Diffusion experiments with numerically integrated isotropic turbulence. *Physics of Fluids*, 1974, **17**, 292–297.
2. McLaughlin, J. B., Aerosol particle deposition in numerically simulated channel flow. *Physics of Fluids*, 1989, **1**, 1211–1224.
3. Squires, K. D. and Eaton, J. K., Preferential concentration of particles by turbulence. *Physics of Fluids*, 1991, **3**(5), 1169–1178.
4. Elghobashi, S. and Truesdell, G. C., Direct simulation of particle dispersion in a decaying isotropic turbulence. *Journal of Fluid Mechanics*, 1992, **242**, 655–700.
5. Wang, L.-P. and Maxey, M. R., Settling velocity and concentration distribution of heavy particles in isotropic turbulence. *Journal of Fluid Mechanics*, 1993, **256**, 27–68.
6. McLaughlin, J. B., Numerical computation of particles–turbulence interaction. *International Journal of Multiphase Flow Suppl.*, 1994, **20**, 211–232.
7. Mashayek, F., Taulbee, D. B. and Givi, P., Modeling and simulation of two-phase turbulent flow. In *Propulsion Combustion*, Chap. 8, ed. G. D. Roy. Taylor and Francis, Washington, D.C., 1998, pp. 241–280.
8. Mashayek, F., Jaberi, F., Miller, R. and Givi, P., Dispersion and polydispersity of droplets in stationary isotropic turbulence. *International Journal of Multiphase Flow*, 1997, **23**(2), 337–355.
9. Laviéville, J., Deutsch, E. and Simonin, O., Large eddy simulation of interactions between colliding particles and a homogeneous isotropic turbulence field. In *Gas–Particle Flows*, ed. D. E. Stock, M. W. Reeks, Y. Tsuji, E. E. Michaelides and M. Gautam. ASME, FED-Vol. 228, 1995, pp. 347–358.
10. Crowe, C. T., Sharma, M. P. and Stock, D. E., The particle-source in cell (PSI-Cell) model for gas–droplet flows. *Journal of Fluids Engineering*, 1977, **6**, 325–332.
11. Wallis, G. B., *One Dimensional Two Phase Flow*. McGraw-Hill, New York, NY, 1969.

12. Bird, R. B., Stewart, W. E. and Lightfoot, E. N., *Transport Phenomena*. Wiley, New York, NY, 1960.
13. Jackson, R. and Davidson, B. J., An equation set for non-equilibrium two phase flow, and an analysis of some aspects of choking, acoustic propagation, and losses in low pressure wet steam. *International Journal of Multiphase Flow*, 1983, **9**(5), 491–510.
14. Givi, P. and Madnia, C. K., Spectral methods in combustion. In *Numerical Modeling in Combustion*, Chap. 8, ed. T. J. Chung, Taylor and Francis, Washington, D.C., 1993, pp. 409–452.
15. Kida, S. and Orszag, S., Energy and spectral dynamics in forced compressible turbulence. *Journal of Scientific Computing*, 1990, **5**(2), 85–125.
16. Balachandar, B. and Maxey, M. R., Methods for evaluating fluid velocities in spectral simulations of turbulence. *Journal of Computational Physics*, 1989, **83**, 96–125.
17. Yeung, P. K. and Pope, S. B., An algorithm for tracking fluid particles in numerical simulations of homogeneous turbulence. *Journal of Computational Physics*, 1988, **79**(2), 373–416.
18. Williams, F. A., *Combustion Theory*, 2nd edn. The Benjamin/Cummings Publishing Company, Menlo Park, CA, 1985.
19. Eaton, J. K. and Fessler, J. R., Preferential concentration of particles by turbulence. *International Journal of Multiphase Flow*, 1994, **20**(Suppl.), 169–209.
20. Blaisdell, G. A., Mansour, N. N. and Reynolds, W. C., Numerical simulation of compressible homogeneous turbulence. Department of Mechanical Engineering Report TF-50, Stanford University, Stanford, CA, 1991.
21. Leonard, A. D. and Hill, J. C., Scalar dissipation and mixing in turbulent reacting flows. *Physics of Fluids A*, 1991, **3**(5), 1286–1299.